Electronic Supplementary Material (ESI) for Materials Horizons.
This journal is © The Royal Society of Chemistry 2019

Supplementary Information for "Negative piezoelectric effect in an organic supramolecular ferroelectric"

Indre Urbanaviciute, Xiao Meng, Michal Biler, Yingfen Wei, Tim D. Cornelissen, Subham Bhattacharjee, Mathieu Linares, Martijn Kemerink

Table of contents

Supplementary methods

I. Device preparation, conditioning and characterization

Device fabrication

Thin film metal-ferroelectric-metal (MFM) capacitor devices for all probed BTA homologues were formed by spin-coating (700–2000 rpm) of a 40 mg/ml chloroform solution on a chemically cleaned glass substrate with patterned aluminum bottom electrodes. Before thermal vacuum deposition of the aluminum top electrodes, spin-coated films were annealed at 70°C for 15 min. to completely evaporate the solvent. The prepared MFM devices were 0.01–1 mm^2 in area. Typical film thickness was 300–700 nm, as measured by a Bruker Dektak XT profilometer.

P(VDF-TrFE) capacitor devices were prepared from 60 mg/ml cyclohexanone solution, which was stirred overnight and filtered before spin-coating at 1000 rpm on patterned chromium/gold (5/50 nm) electrodes on chemically cleaned glass substrates. Deposited films were annealed at 140 °C for 2 hours to increase crystallinity. Top gold electrodes were subsequently deposited by thermal evaporation in vacuum to form cross-bar structure capacitor devices. Ferroelectric devices were further characterized as described below.

Homeotropic alignment procedure

In the as-cast organic ferroelectric film BTA molecular columns lie in-plane to the electrode[1]. When molecular dipoles are oriented in this way, no polarization can be measured in the bottom-top electrode geometry. Therefore, prior to the electrical measurements the devices are treated by a field annealing procedure,[2,3] when at low viscosity conditions (≈70–100 °C) with the help of an alternating external field molecular bundles are forced to stand perpendicularly to the electrodes. The procedure (see Figure 4 of the main text) takes 10–180 seconds, and accelerates with the applied field, its frequency and temperature. The subsequent field cooling freezes the system in this quasi-orderly state. Due to π-stacking of the benzene core and hydrogen bonding of the amide groups, accompanied by alkyl chain freezing, the hexagonal packing remains stable even without external field. This has been previously tested by polarized light optical microscopy (POM) and can be seen from unchanged current transients corresponding to polarization reversal after a long waiting time.[4] Therefore only the polarization switching current, rising from the dipole rotation, reflects in the quasi-statically measured *P-E* curves, once the device is properly conditioned. The broadness of the switching kinetics corresponds to the level of structural disorder in the active layer.

Ferroelectric characterization

The polarization loops are obtained by integration of the switching current transients. We use a quasi-static mode, better known as the Double Wave Method (DWM),[5] when non-switching current is subtracted from the initial signal to avoid displacement and leakage inputs in the *P-E* curves. The input signal waveform is supplied by a Tektronix AFG3000 Arbitrary Function Generator and is amplified by a TREK PZD350A high voltage amplifier. The device response is visualized by a Tektronix TBS1000B Digital Oscilloscope.

Piezoelectric characterization

Interferometry-based measurement techniques are a classical approach to characterize piezoelectric ceramics as well as thin-films by probing the converse piezoelectric response [6,7]. Being entirely contactless, the optical probe of the double-beam laser interferometer (DBLI) does not interact mechanically with the film, thus the response is measured with real electrodes in macroscopic, real-device conditions. In case of PFM, the piezoelectric response is probed locally and is induced by the sharp tip, which complicates the estimation of the magnitude of the local applied field and makes the measurement vulnerable to surface states/defects. Due to this, multiple studies question the validity of piezoresponse force microscopy[8]. In addition, the PFM probing mechanism only allows obtaining data at small-signal conditions, while DBLI allows to probe both the large-signal and small-signal response, and therefore is strongly preferred for our purposes.

The interferometric approach of the DBLI enables high precision measurements with angstrom accuracy. A vibration damping system is used to reduce the environmental noise. The equipment is of sufficient sensitivity and precision to measure the piezoelectric response in thin-films that typically give only small displacements, in the range of picometers.

Compared to single-beam systems, the second reference laser beam (Mach–Zehnder interferometer) allows to compensate for possible substrate bending artefacts due to lateral piezoelectric activity. This is especially important for inorganic piezoelectric thin-films that are strongly clamped (usually, grown directly) on the substrate and have high piezoelectric constants. In case of organic piezoelectrics, this issue is less likely due to the very different physical properties of the film and the substrate and the rather weak mechanical coupling.

One important condition to get accurate results with the DBLI is the high reflectivity of both the top and bottom electrodes. In our case of glass/Al/BTA/Al (as well as glass/Cr/Au/P(VDF-TrFE)/Au) devices, the thermally evaporated aluminium (gold) electrodes act as practically perfect mirrors. This is possible due to the typically very low surface roughness (of a few nanometres) of the BTA layers. An image of a typical sample can be found in Supplementary Figure 2c.

As mentioned above, due to the mechanical clamping of the piezoelectric layers on the substrate, the limited in-plane strain (corresponding to d_{31}) can effectively reduce the out-of-plane strain, as d_{31} and d_{33} are related by Poisson's ratio. The factually measured longitudinal piezoelectric coefficients are thus referred to as 'effective' and are typically lower than the real value for an unclamped film. Otherwise, the technique has no limitations for repeatability and stable results are obtained.

II. Introduction to piezoelectric constants and mechanisms

Piezostriction

A piezoelectric material can be characterized by several coefficients quantifying its direct and converse electromechanical response. In the phenomenological model based on the thermodynamic definition, the piezoelectric response is assumed to result from the polarization-coupled-electrostriction (piezostriction), as shown in Eq.1 of the main text. Four main piezoelectric constants with relations to the electrostrictive coefficients are given below.[7,9] A simplified representation excluding tensors is used, noting that only the 33 mode is relevant for the paper.

$$d = \left(\frac{\partial D}{\partial X}\right)_E = \left(\frac{\partial S}{\partial E}\right)_X = 2\varepsilon_r\varepsilon_0 Q P_r = \varepsilon_r\varepsilon_0 g$$

$$g = -\left(\frac{\partial E}{\partial X}\right)_D = \left(\frac{\partial S}{\partial D}\right)_X = 2QP_r$$

$$e = \left(\frac{\partial D}{\partial S}\right)_E = -\left(\frac{\partial X}{\partial E}\right)_S = 2\varepsilon_r\varepsilon_0 \gamma P_r = \varepsilon_r\varepsilon_0 h$$

$$h = -\left(\frac{\partial E}{\partial S}\right)_D = -\left(\frac{\partial X}{\partial D}\right)_S = 2\gamma P_r$$

The first and second terms in brackets correspond to the direct and converse effect, respectively. The basic relations of the coefficients with mechanical properties are given by:

$$\gamma = Q \cdot Y$$

$$e = d \cdot Y$$

$$h = g \cdot Y$$

$$\nu = \frac{d_{31}}{d_{33}}$$

Here, D is electric displacement, E – electric field, $\varepsilon_r\varepsilon_0$ – dielectric permittivity of a piezoelectric, γ – electrostrictive coupling coefficient, ν – Poisson ratio, P_{r} – remnant polarization, Q – electrostriction coefficient, S – strain, X – stress and Y – Young's modulus.

Based on the equations given above it is evident that all other piezoelectric coefficients can be derived if one of the constants and the mechanical properties are known. In Supplementary Table 1 we show the calculated values of all the relevant constants from three independently measured coefficients: the piezoelectric constants d_{33} and g_{33}, and the electrostriction coefficient Q_{33}. The piezoelectric coefficient d_{33} was obtained from large-signal strain-field characteristics (Figure 2a). The electrostriction coefficient Q_{33} was extracted from the strain-displacement representation of the data (Supplementary Figure 3). The piezoelectric constant g_{33} resulted from the low-field measurements, specifically the strain-displacement plot (Supplementary Figure 7), based on the analysis presented in Ref. [7] for PVDF and its copolymers. All the calculated values are closely matching, which proves that piezostriction is the dominant factor for highly ordered devices of BTA-C6.

Dimensional effect

One of the most studied and utilized piezoelectric materials with the negative piezoelectric effect is the ferroelectric copolymer P(VDF-TrFE). With a remnant polarization of 60–120 mC/m^2, a piezoelectric coefficient d_{33} of −20–−40 pm/V and utile physical properties, P(VDF-TrFE) is an attractive choice for ferroelectric and piezoelectric applications in both conventional and flexible electronics[10–12]. Since the discovery of the negative piezoelectricity in PVDF roughly 50 years ago[13], multiple attempts to determine the underlying processes have been reported. The phenomenon has been studied theoretically and experimentally in single polymer chains, in ideal crystallites and in macroscopic semi-crystalline (crystalline + amorphous) systems. Density functional theory (DFT) calculations on individual polymer chains revealed that the PVDF backbone stretches when the electric field is applied in the polarization direction, which leads to chain compression[14]. Molecular dynamics (MD) simulations on pseudo-hexagonally packed polymer chains within crystallites also resulted in negative strain with applied field[15]. This was confirmed experimentally by in-situ XRD measurements when the lattice parameters were monitored upon polarization reversal in P(VDF-TrFE) thin-films[16]. Interestingly, every suggested explanation resulted in piezoelectric coefficient estimates that matched the experimentally obtained value of around −30 pm/V, highlighting the complexity of the problem.

Generally, the negative piezoelectric effect in P(VDF-TrFE) is explained by the dimensional effect[7,9,17]. It considers the ferroelectric layer as a set of rigid dipoles that are distributed in a deformable matrix (i.e. with Poisson ratio $v < 0.5$). As polarization P is the total dipole M density $P = \frac{M}{V} = \frac{M}{Ad}$, where V is volume, A is area and d is thickness of the device, compression of the device results in increased polarization. This is a very straightforward explanation for the direct negative piezoelectric effect. It holds for the macroscopic P(VDF-TrFE) device perspective, as an intermixture of crystalline and amorphous matter, as well as for the microscopic device perspective, where rigid polymer chains within crystallites are held together by weak van der Waals interactions. This is very different from the 'conventional' piezoelectricity in, e.g., inorganic perovskites or organic crystals, where the effect is positive and essentially governed by the lattice expansion upon applied electric field.

Furukawa *et al.* constructed a simplified model to calculate piezoelectric constants, which assumes that mechanical deformation only results in a change in the layer thickness, with all other parameters remaining constant. This leads to the description of piezo-parameters as given in Supplementary Table 1, bottom rows. While, based on Ref. [7,9], for P(VDF-TrFE) the values calculated in this way are largely consistent with the ones obtained experimentally, this is not the case for BTA-C6. The predicted coefficients are two to five times larger than the experimentally obtained ones. Despite the fact that, supposedly, for BTA-C6 the assumptions of the model do not fully hold (e.g. in terms of Poisson ratio), the dimensional effect can be considered as a dominant factor for the piezoelectric activity of this material.

Simulated BTA strain-field trends at the nanoscale

The BTA-C1 molecule was optimized within the DFT formalism using the Gaussian software package[19]. The Ante_R.E.D. program[20–22] with B3LYP/cc-pVDZ was used to calculate ESP charges. Then, the BTA self-assembly was constructed in a 3:0 rotamer made of 18 BTA molecules in the stack to ensure periodic boundary conditions in *z*-direction, for which topology and initial coordinate files were generated by the LEaP program with general amber force field (GAFF)[23]. MD simulations ran in NVT ensemble at 300 K using Langevin dynamics for 40 ns with a time step of 2 fs per step, the trajectories were recorded every 5000 steps and the cut-off was set to 12 Å for non-bonded interactions. The box size was scanned from 62.75 to 59.5 Å with a step of 0.25 Å, and from 59.5 to 58 Å with a 0.5 Å step. First, simulations ran without applying an electric field. Then, a series of electric fields with different strengths were applied: 0.11 and 0.22 V/nm in both directions as neither of the strengths are high enough to induce the flip in the time of our simulations, and 0.43, 0.65, and 0.87 V/nm in only the preferred positive direction, which does not induce any dipole flipping, just strain. To evaluate energetics of the system, the sum of van der Waals and electrostatic energies were extracted for each box size and electric field and recalculated per one BTA molecule. The sum shown here corresponds to the average energy during the whole MD simulations to ensure better sampling, although the averages of the sums for every 10 ns (0–10 ns, 10–20 ns, 20–30 ns, 30–40 ns) change inconsiderably. All MD simulations were carried out using the Amber 16 software package[24].

Piezostriction vs. Maxwell strain

The linear negative piezostriction and the quadratic Maxwell strain are both present in ferroelectric films and are in principle competing mechanisms. The balance between these mechanisms is determined by the ferroelectric polarization and Young's modulus. Given $S_{33,\ Maxwell} = -\frac{\varepsilon_r \varepsilon_0}{2Y} E^2$ and $S_{33,\,Piezostrictive} = (2Q_{33}\varepsilon_r \varepsilon_0 P_r)E$, the ratio of the two is $S_{33,\ Maxwell}/S_{33,\,Piezostrictive} = \frac{1}{4Y_{33}Q_{33}P_r}E$, which leads to piezostriction (Maxwell strain) being dominant at fields lower (higher) than $4Y_{33}Q_{33}P_r$. This is illustrated in Supplementary Figure 14 for each BTA homologue. The higher the $Y_{33}Q_{33}P_r$ coefficient, the less likely it is for the device to enter the Maxwell-strain dominated field-range in normal operation conditions (close to coercive fields). While for shorter-substituted BTA homologues this critical field (vertical dotted lines) is far above the coercive field, for longer-tailed BTAs these mechanisms become strongly competing, with an extreme example of BTA-C18 where the critical field is actually smaller than the coercive field. This trend of Maxwell strain becoming more pronounced for longer-substituted BTA's is clearly reflected in Supplementary Figure 11 as an increasingly distorted and quadratic strain-voltage relation.

Supplementary Tables

Supplementary Table 1. Piezoelectric constants of BTA-C6 devices. Piezoelectric coefficients of highly-ordered BTA-C6, calculated from three independently experimentally obtained constants – d_{33}, Q_{33} and g_{33}, and from the simplified dimensional effect formalism. Coefficient relations result from the thermodynamic definition based on electrostriction. Experimentally obtained values are indicated in bold. Constant remnant polarization $P_r = 55$ mC/m^2, Young's modulus $Y_{33} = 1.5$ GPa and relative dielectric permittivity $\varepsilon_r = 7$ were used for calculations.

From experimental d_{33}					
$Q_{33} = \frac{d_{33}}{2\varepsilon_r\varepsilon_0 P_r}$	$\gamma_{33} = \frac{d_{33}Y_{33}}{2\varepsilon_r\varepsilon_0 P_r}$	**Exp. d_{33}**	$g_{33} = \frac{d_{33}}{\varepsilon_r\varepsilon_0}$	$h_{33} = \frac{d_{33}Y_{33}}{\varepsilon_r\varepsilon_0}$	$e_{33} = d_{33}Y_{33}$
−1.03 m^4/C^2	$-1.54\cdot10^{9}$ a. u.	**−7 pm/V**	−0.113 m^2/C	$-1.69\cdot10^{8}$ a. u.	−0.01 C/m^2
From experimental Q_{33}					
Exp. Q_{33}	$\gamma_{33} = Q_{33}Y_{33}$	$d_{33} = 2\varepsilon_r\varepsilon_0 Q_{33}P_r$	$g_{33} = 2Q_{33}P_r$	$h_{33} = 2Q_{33}Y_{33}P_r$	$e_{33} = 2\varepsilon_r\varepsilon_0 Q_{33}Y_{33}P_r$
−1 m^4/C^2	$-1.5\cdot10^{9}$ a. u.	−6.8 pm/V	−0.11 m^2/C	$-1.65\cdot10^{8}$ a. u.	−0.01 C/m^2
From experimental g_{33}					
$Q_{33} = \frac{g_{33}}{2P_r}$	$\gamma_{33} = \frac{g_{33}}{2P_r}Y_{33}$	$d_{33} = \varepsilon_r\varepsilon_0 g_{33}$	**Exp.** g_{33}	$h_{33} = g_{33}Y_{33}$	$e_{33} = \varepsilon_r\varepsilon_0 g_{33}Y_{33}$
−0.95 m^4/C^2	$-1.42\cdot10^{9}$ a. u.	−6.44 pm/V	**−0.1 m^2/C**	$-1.56\cdot10^{8}$ a. u.	−0.0097 C/m^2
Dimensional effect formalism, based on Ref. [7,9]					
$Q_{33} = -\frac{1}{2\varepsilon_r\varepsilon_0 Y_{33}}$	$\gamma_{33} = -\frac{1}{2\varepsilon_r\varepsilon_0}$	$d_{33} = -P_r/Y_{33}$	g_{33}	h_{33}	$e_{33} = -P_r$
−5.4 m^4/C^2	$-8.1\cdot10^{9}$ a. u.	−36.7 pm/V	−0.59 m^2/C	$-8.88\cdot10^{8}$ a. u.	−0.055 C/m^2

Supplementary Figures

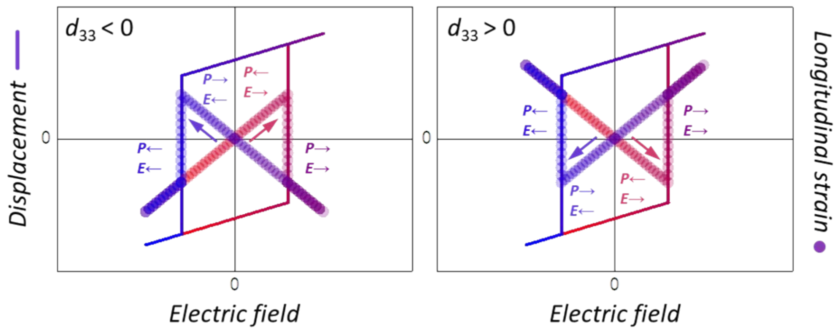

Supplementary Figure 1. Schematics of piezostrictive strain for the ideal negative and positive converse piezoelectric effect. In the case of negative piezoelectricity (left), the layer linearly contracts when polarization and field directions match and expands when they are opposite, corresponding to negative d_{33}. The positive piezoelectricity (right) leads to similar yet inverted characteristics and positive d_{33}.

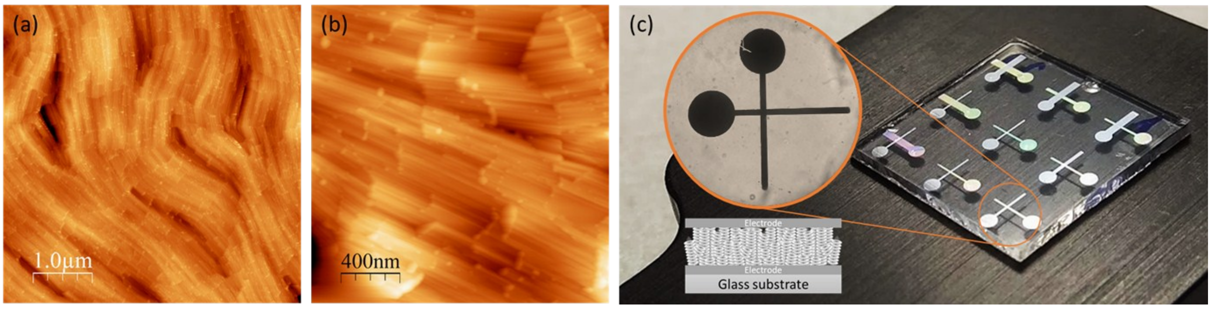

Supplementary Figure 2. AFM micrographs of an as-deposited BTA-C6 film and typical devices. (a,b) Long self-assembled supramolecular structures are observed in-plane to the substrate at the nanoscale after spin-coating from solution, as observed by AFM. These molecular columns can be reoriented homeotropically by a mild field-annealing procedure as described in the main text (Figure 4), which is typically shorter than poling of polycrystalline ferroelectric materials. (c) A prepared 9-device sample (15×15 mm^2) with crossbar-structure aluminum electrodes (circular pads are there to conveniently connect the probe needles). A side-view of the contact area is given in the inset. BTAs form smooth (nanometer-range surface roughness) transparent thin-films after spin-coating from solution, which allows for a nearly perfect reflectivity of the deposited electrodes and guarantees good quality DBLI measurement results.

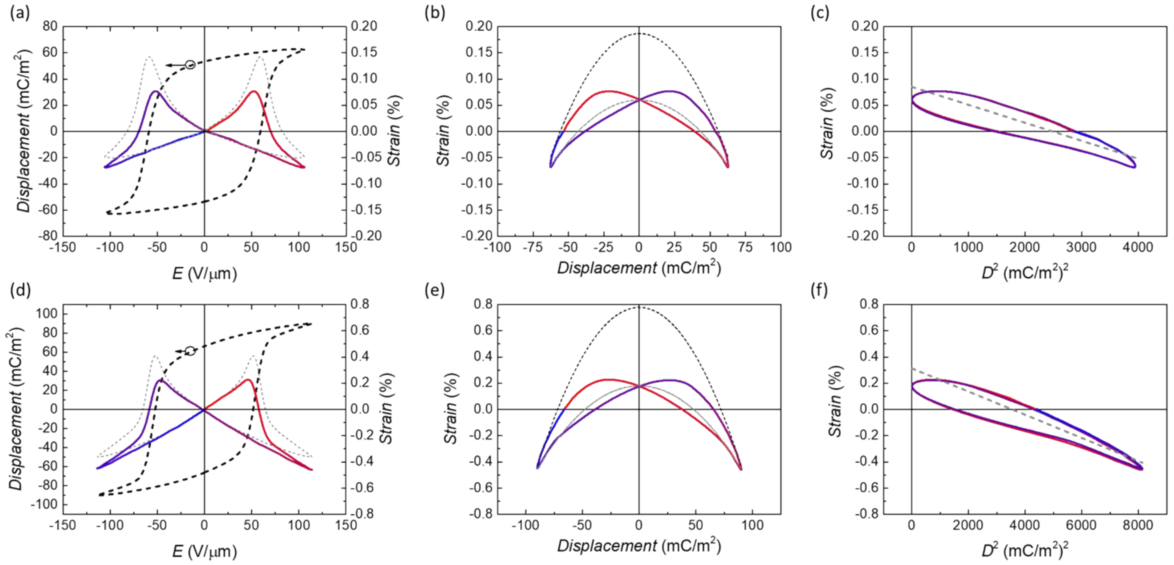

Supplementary Figure 3. Fitting the electrostriction coefficient Q_{33} for BTA-C6 and P(VDF-TrFE). (a,d) Strain-field *S-E* and displacement-field *D-E*, (b,e) strain-displacement *S-D* and (c,f) strain-displacement squared *S-*D^2 characteristics of BTA-C6 and P(VDF-TrFE), respectively. Dashed grey lines are fits to $S \sim Q_{33} \cdot D^2$ with $Q_{33} = -0.55$–-1 m^{4}C^{-2} for BTA and $Q_{33} = -0.8$–-1.5 m^{4}C^{-2} for P(VDF-TrFE).

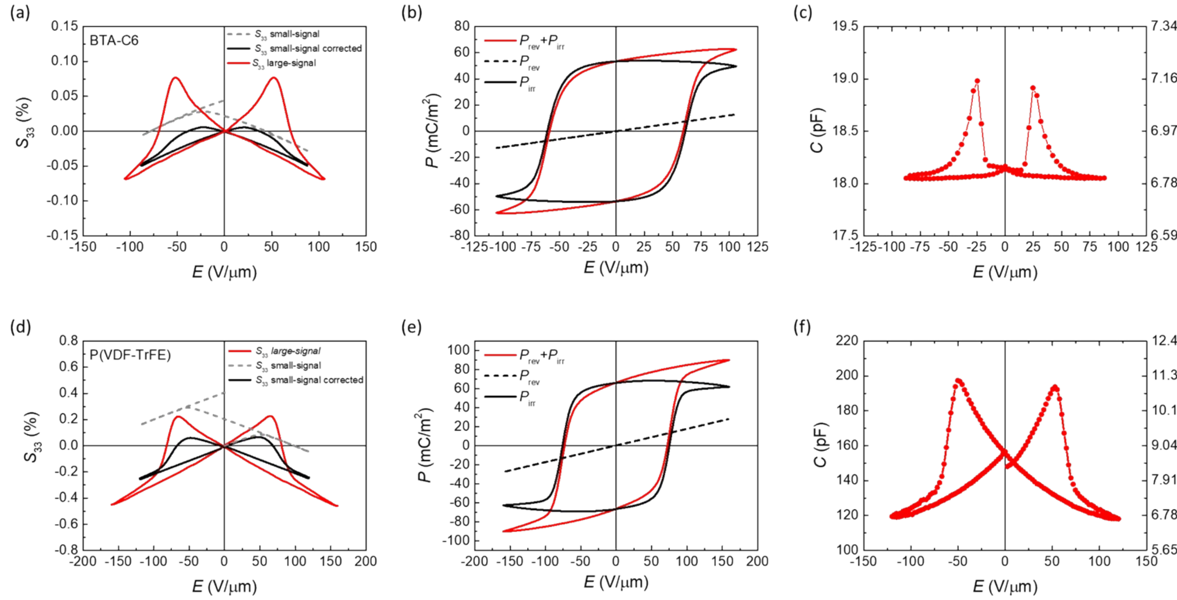

Supplementary Figure 4. Small- and large-signal characteristics of BTA-C6 and P(VDF-TrFE). Comparison of small- and large-signal response of (a–c) an average BTA-C6 device and (d–f) a P(VDF-TrFE) device. (a,d) Large-signal (red line) and small-signal (dashed grey line) strain, obtained by integration of the measured small-signal d_{33}-*E* characteristics. The black solid line is the small-signal strain corrected for the effect of irreversible polarization.

Different slow sweep frequencies were used for *LS* and *SS*, leading to non-matching peak positions. (b,e) Total large-signal polarization (red line), reversible polarization part (black dashed line) obtained from the integrated *C*-*V* data of the panels (c,f), and the irreversible polarization (black solid line) obtained by subtraction of the former two. (c,f) Capacitance-field characteristics with corresponding relative permittivity ε_r. When integrated, these characteristics give only slight hysteresis with polarization values lower than 0.1 mC/m^2 for BTA-C6 and 1 mC/m^2 for P(VDF-TrFE).

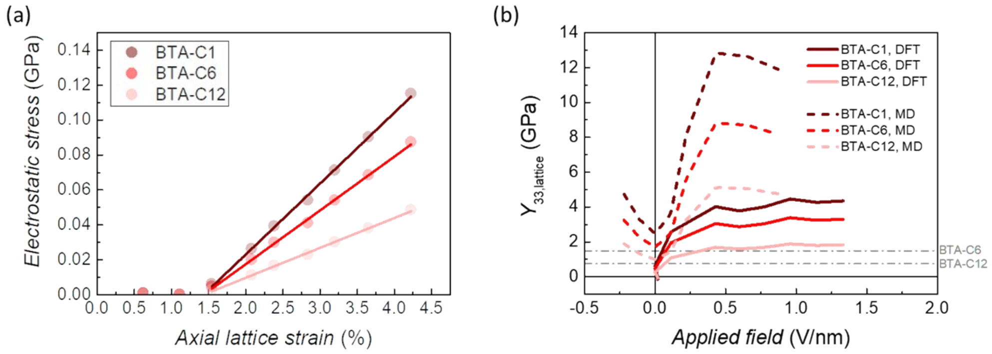

Supplementary Figure 5. Simulated axial elastic moduli for BTAs. (a) Electrostatic stress-strain characteristics from DFT computations on a BTA dimer, calculated for different molecular packings, corresponding to BTA-C1, BTA-C6 and BTA-C12. Linear fits give $Y_{33,\text{lattice}}$ of 1.7 GPa, 3.1 GPa and 4.1 GPa, respectively. (b) Nanoscopic axial lattice Young's modulus calculated using different approaches. Solid lines result from the electrostatic stress approach and are derivatives of the DFT data in panel (a). Dashed lines are derived from the MD data in Figure 3b. Grey horizontal dash-dotted lines indicate values extracted from the experimental data at 60°C. The results for BTA-C1 were obtained directly from the simulations, while data for BTA-C6 and BTA-C12 was recalculated using typical molecular packing parameters. An intercolumnar distance of 1.35 nm, 1.55 nm and 2.08 nm was used in calculations for BTA-C1, BTA-C6 and BTA-C12, respectively[1].

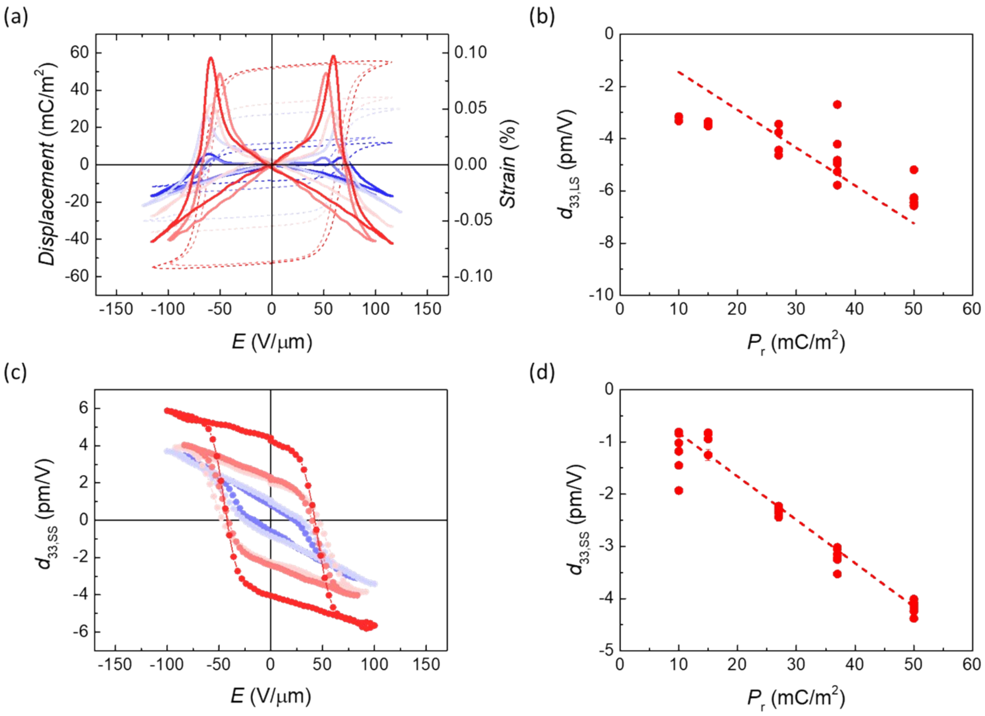

Supplementary Figure 6. BTA-C6 samples with different homeotropic alignment levels. (a) Polarization- and strain-field characteristics of BTA-C6 samples with different homeotropic alignment levels (see Figure 4 of the main text for details). (b) Corresponding large-signal d_{33} values plotted over the remnant polarization P_r. Linear fitting gives ~0.15 pm/V growth per 1 mC/m^2. (c) Small-signal d_{33} versus applied field loops and (d) zero-field $d_{33,SS}$ dependence on remnant polarization, with 0.085 pm/V per 1 mC/m^2 slope.

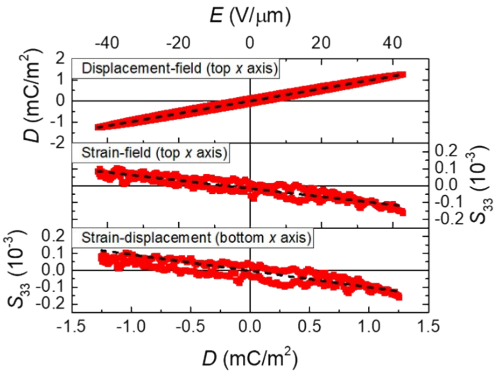

Supplementary Figure 7. Measuring the piezoelectric constant g_{33} in BTA-C6. Displacement-field (top), strain-field (middle) and, the combination of the two, displacement-strain (bottom) characteristics measured at low-field conditions for evaluation of the piezoelectric g_{33} constant of BTA-C6. The slope of the *S*-*D* plot gives $g_{33} = -0.1$ m^2/C.

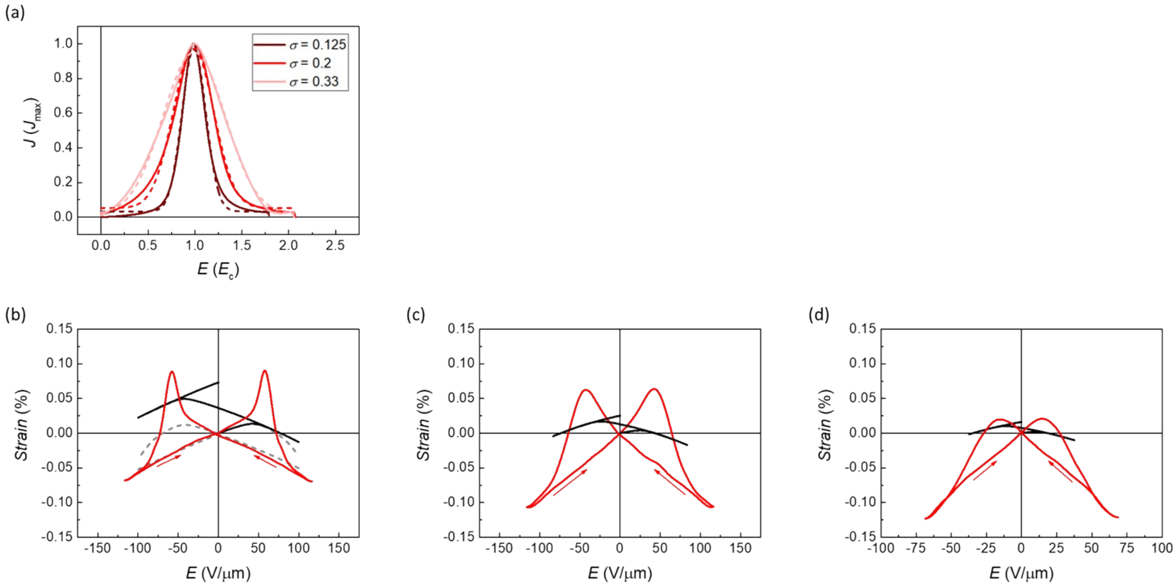

Supplementary Figure 8. Strain-field butterfly loops versus disorder for BTA-C6. (a) An example of switching current transients of BTA-C6 with three different σ values as obtained from Gaussian fits. (b–d) LS (red lines) and SS (integrated $d_{33,\mathrm{SS}}$, black lines) strain-field characteristics of BTA-C6 samples with increasing disorder from (b) to (d). While close-to-ideal loops are found for low-disorder devices (such as in panel (b)), more elongated and blunt loops are characteristic for higher-disorder samples, e.g. panels (c,d). However, higher-disorder devices give more strain, which results mostly from extrinsic effects. This can be seen as a larger mismatch between the slopes of the small-signal (black lines) and large-signal (red lines) strains.

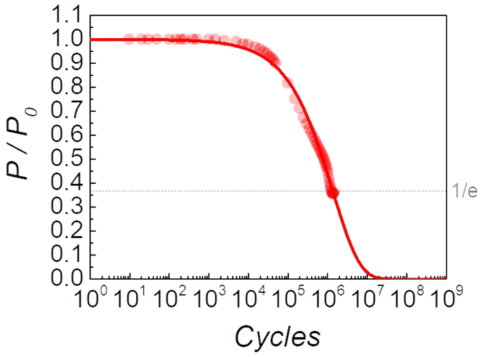

Supplementary Figure 9. Electrical fatigue of a non-optimized BTA-C6 device. Fatigue characteristics is measured for full polarization switching ($\pm P_\mathrm{s}$) using bipolar triangular electric field signal of amplitude exceeding the coercive field more than twice, $E_\mathrm{max} > 2E_\mathrm{c}$. The trend is fitted to a stretched exponential function with a stretching exponent of 0.6 and a constant of ~$1.5\cdot10^6$ cycles. For optimized device and unipolar field sweeping, which is typical for piezoelectric applications, a slower fatigue is expected.

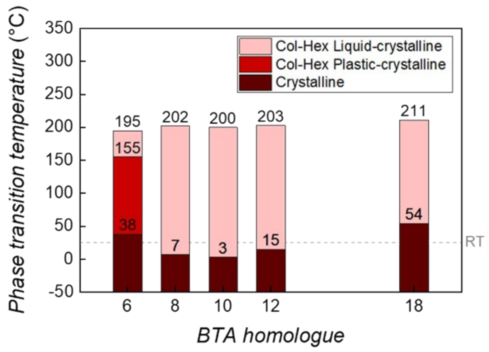

Supplementary Figure 10. Phase transition temperature points for different BTA homologues. Data for the first cooling cycle. Corresponding DSC curves can be found in Ref. 1. A columnar-hexagonal liquid crystalline phase is found for all homologues at and above room temperature. In the 38–155°C temperature range, BTA-C6 demonstrates a higher degree of order compared to the other homologues, which manifests itself as additional Bragg diffraction peaks in the WAXS diffractograms and might indicate a columnar-hexagonal lattice with tilted columns[3]. We refer to this phase as plastic crystalline.

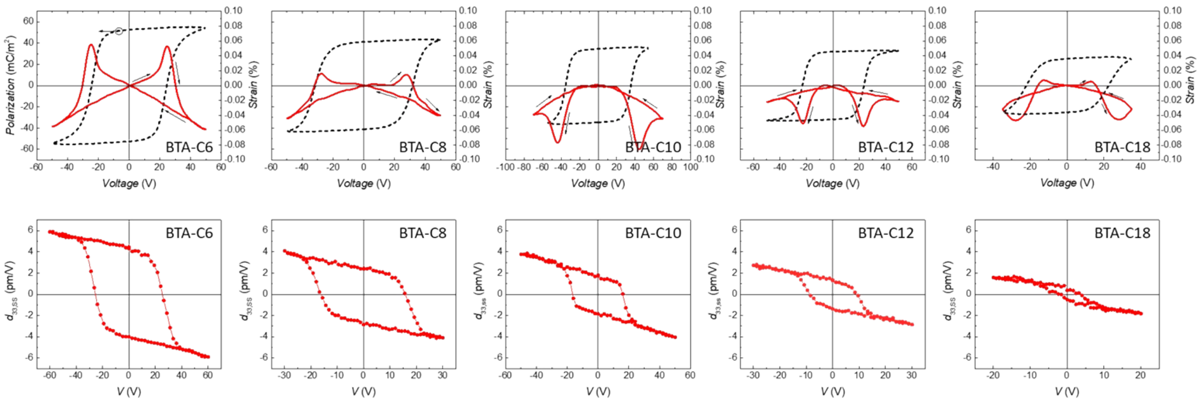

Supplementary Figure 11. Piezoelectric response of all BTA homologues. Typical large-signal strain-voltage (top row) and small-signal (bottom row) d_{33} versus voltage characteristics of different BTA homologues. From left to right: C6, C8, C10, C12 and C18. The *y*-axes scale is kept the same for all panels. While C6 and C8 demonstrate a regular, albeit negative, piezoelectric butterfly, longer-substituted BTA-C10 (with rare exceptions), C12 and C18 have contraction-only electromechanical response, which is mostly governed by the Maxwell stress, enhanced by softening of the material upon polarization switching. Based on fits, the extracted Young’s modulus increases steadily for shorter-substituted BTAs: 0.3

GPa for BTA-C18, 0.75 GPa for BTA-C12 and 0.95 GPa for BTA-C10. From this trend the extrapolated Y_{33} values for BTA-C8 and BTA-C6 are 1.2 GPa and 1.5 GPa, respectively. The small-signal response remains normal for all BTA homologues with gradually decreasing piezoelectric coefficient with lengthening of the alkyl chains, as discussed in the main text.

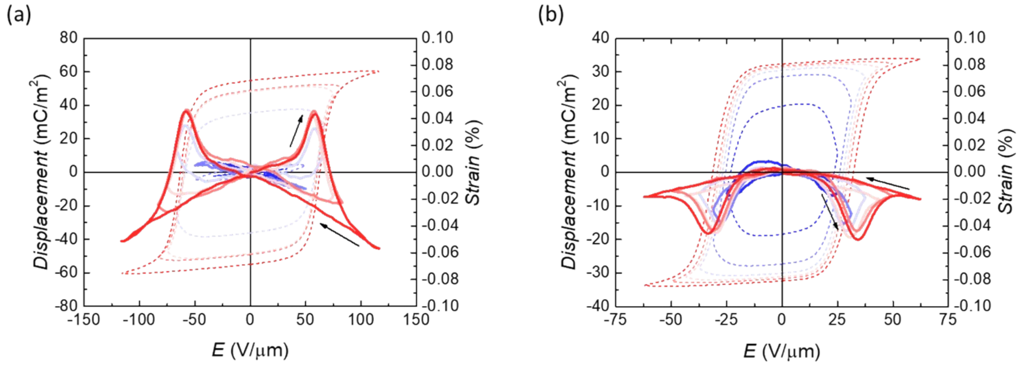

Supplementary Figure 12. Partial switching characteristics in BTAs. *S*-*E* and *P*-*E* characteristics with inner loops for (a) BTA-C6 and (b) BTA-C12. Inner loops do not fit into each other precisely due to small differences in probing frequency.

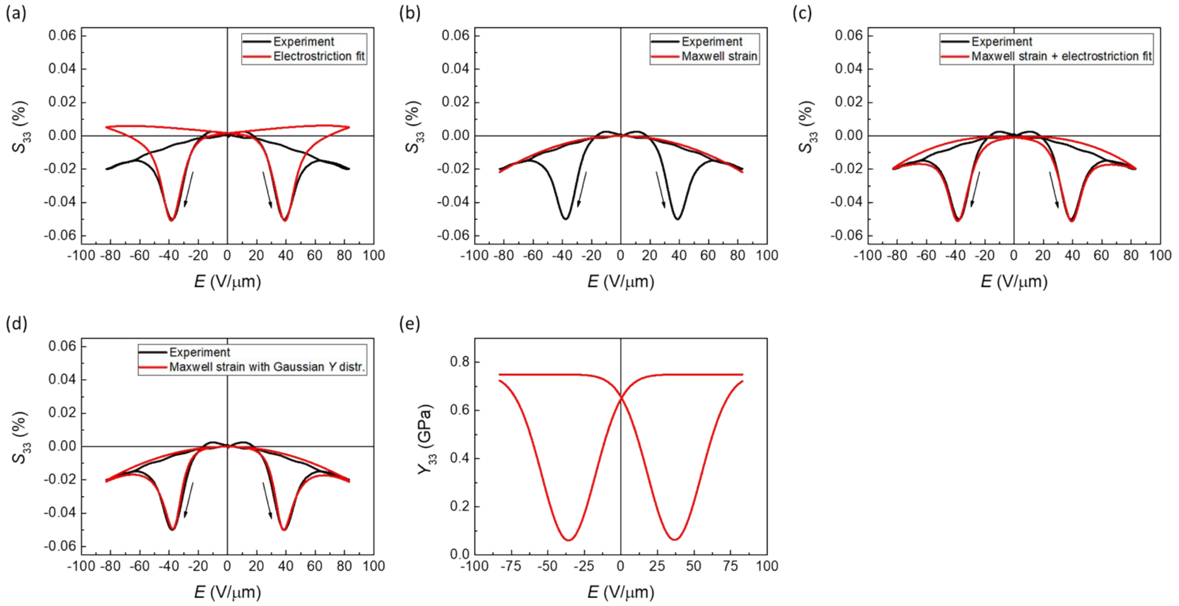

Supplementary Figure 13. Different fitting variants for *S-E* loops of longer-substituted BTAs, BTA-C12 is used as an example. (a) Fitting to the electrostriction model $S_{33} = Q_{33}D^2$ (using a measured *D*-*E* hysteresis loop) with a positive $Q_{33} = +0.55$ m^4/C^2. (b) Maxwell strain with a constant Young's modulus $Y_{33} = 0.75$ GPa. (c) Fitting using a combination of the Maxwell strain and the electrostriction formulae: $Q_{33} = +0.52$ m^4/C^2, $Y_{33} = 0.7$ GPa. (d) Maxwell strain with a Gaussian distribution of the Young's modulus (seen in panel (e)), with

0.75 GPa when fully poled and 0.65 GPa at zero field. The fitted minimum Y value at the coercive field (randomized polarization point) was ~0.06 GPa.

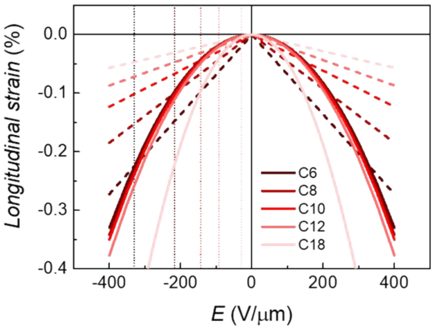

Supplementary Figure 14. Competing electromechanical response mechanisms in BTAs. Linear piezostrictive strain $S_{33,\,Piezostrictive} = (2Q_{33}\varepsilon_r\varepsilon_0P_r)E$ (dashed lines) and quadratic Maxwell strain $S_{33,\ Maxwell} = -\frac{\varepsilon_r\varepsilon_0}{2Y}E^2$ (solid lines) are simultaneously present in ferroelectric films. The balance between the ferroelectric polarization and the Young's modulus determines which mechanism is dominant at a particular range of applied fields. The critical field (vertical dotted lines) after which the Maxwell strain conquers the piezostrictive strain is $4Y_{33}Q_{33}P_r$.

Supplementary References

1. Urbanaviciute, I. *et al.* Tuning the Ferroelectric Properties of Trialkylbenzene-1,3,5-tricarboxamide (BTA). *Adv. Electron. Mater.* **3,** 1600530 (2017).

2. Fitié, C. F. C., Roelofs, W. S. C., Kemerink, M. & Sijbesma, R. P. Remnant polarization in thin films from a columnar liquid crystal. *J. Am. Chem. Soc.* **132,** 6892–6893 (2010).

3. Fitié, C. F. C. *et al.* Polar Switching in Trialkylbenzene-1,3,5-tricarboxamides. *J. Phys. Chem. B* **116,** 3928–3937 (2012).

4. Gorbunov, A. V. *et al.* Polarization loss in the organic ferroelectric trialkylbenzene-1,3,5-tricarboxamide (BTA). *Phys. Chem. Chem. Phys.* **19,** 3192–3200 (2017).

5. Gorbunov, A. V. *et al.* True ferroelectric switching in thin films of trialkylbenzene-1,3,5-tricarboxamide (BTA). *Phys. Chem. Chem. Phys.* **18,** 23663–23672 (2016).

6. Pan, W. Y. & Cross, L. E. A sensitive double beam laser interferometer for studying high-frequency piezoelectric and electrostrictive strains. *Rev. Sci. Instrum.* **60,** 2701–2705 (1989).

7. Furukawa, T. & Seo, N. Electrostriction as the origin of piezoelectricity in ferroelectric polymers. *Jpn. J. Appl. Phys.* **29,** 675–680 (1990).

8. Vasudevan, R. K., Balke, N., Maksymovych, P., Jesse, S. & Kalinin, S. V. Ferroelectric or non-ferroelectric: Why so many materials exhibit ‘ferroelectricity’ on the nanoscale. *Appl. Phys. Rev.* **4,** 21302 (2017).

9. Furukawa, T. Piezoelectricity and pyroelectricity in polymers. *IEEE Trans. Electr. Insul.* **24,** 375–394 (1989).

10. Khikhlovskyi, V. *et al.* Multi-bit organic ferroelectric memory. *Org. Electron.* **14,** 3399–3405 (2013).

11. Lang, S. B. & Muensit, S. Review of some lesser-known applications of piezoelectric and pyroelectric polymers. *Appl. Phys. A* **85,** 125–134 (2006).

12. Pi, Z., Zhang, J., Wen, C., Zhang, Z. & Wu, D. Flexible piezoelectric nanogenerator made of poly(vinylidenefluoride-co-trifluoroethylene) (PVDF-TrFE) thin film. *Nano Energy* **7,** 33–41 (2014).

13. Kawai, H. The Piezoelectricity of Poly (vinylidene Fluoride). *Jpn. J. Appl. Phys.* **8,** 975–976 (1969).

14. Bystrov, V. S. *et al.* Molecular modeling of the piezoelectric effect in the ferroelectric polymer poly(vinylidene fluoride) (PVDF). *J. Mol. Model.* **19,** 3591–3602 (2013).

15. Zhu, G., Zeng, Z., Zhang, L. & Yan, X. Piezoelectricity in β-phase PVDF crystals: A molecular simulation study. *Comput. Mater. Sci.* **44,** 224–229 (2008).

16. Katsouras, I. *et al.* The negative piezoelectric effect of the ferroelectric polymer poly(vinylidene fluoride). *Nat. Mater.* **15,** 78–84 (2016).

17. Broadhurst, M. G., Davis, G. T., McKinney, J. E. & Collins, R. E. Piezoelectricity and pyroelectricity in polyvinylidene fluoride—A model. *J. Appl. Phys.* **49,** 4992–4997 (1978).

18. Kulkarni, C., Reddy, S. K., George, S. J. & Balasubramanian, S. Cooperativity in the stacking of benzene-1,3,5-tricarboxamide: The role of dispersion. *Chem. Phys. Lett.* **515,** 226–230 (2011).

19. Gaussian 09, Revision D.01, M. J. Frisch, G. W. Trucks, H. B. Schlegel, G. E. Scuseria, M. A. Robb, J. R. Cheeseman et al., Gaussian, Inc., Wallingford CT, 2013.

20. Vanquelef, E. *et al.* R.E.D. Server: a web service for deriving RESP and ESP charges and building force field libraries for new molecules and molecular fragments. *Nucleic Acids Res.* **39,** W511–W517 (2011).

21. Pigache, A., Cieplak, P., Dupradeau, F.-Y. Automatic and highly reproducible RESP and ESP charge derivation: Application to the development of programs RED and X RED. 227th ACS National Meeting, Anaheim, CA, USA, March 28 - April 1 (2004).

22. Dupradeau, F.-Y. *et al.* The R.E.D. tools: advances in RESP and ESP charge derivation and force field library building. *Phys. Chem. Chem. Phys.* **12,** 7821 (2010).

23. Wang, J., Wolf, R. M., Caldwell, J. W., Kollman, P. A. & Case, D. A. Development and testing of a general amber force field. *J. Comput. Chem.* **25,** 1157–1174 (2004).

24. D.A. Case, R.M. Betz, D.S. Cerutti, T.E. Cheatham, III, T.A. Darden, R.E. Duke, T.J. Giese, H. Gohlke, A.W. Goetz, N. Homeyer, S. Izadi, P. Janowski, *et al.* AMBER 2016, University of California, San Francisco (2016).